Monthly Notices
of the
ROYAL ASTRONOMICAL SOCIETY

MNRAS **485,** 2573–2588 (2019)
Advance Access publication 2019 February 20

doi:10.1093/mnras/stz517

The 'Big Dipper': the nature of the extreme variability of the AGN SDSS J2232−0806

Daniel Kynoch,[1]★ Martin J. Ward,[1] Andy Lawrence,[2] Alastair G. Bruce,[2] Hermine Landt[1] and Chelsea L. MacLeod[3]

[1]*Centre for Extragalactic Astronomy, Department of Physics, Durham University, South Road, Durham DH1 3LE, UK*
[2]*Institute for Astronomy, SUPA (Scottish Universities Physics Alliance), University of Edinburgh, Royal Observatory, Blackford Hill, Edinburgh EH9 3HJ, UK*
[3]*Harvard-Smithsonian Center for Astrophysics, 60 Garden Street, Cambridge, MA 02138, USA*

Accepted 2019 February 14. Received 2019 February 14; in original form 2018 November 30

ABSTRACT

SDSS J2232−0806 (the 'Big Dipper') has been identified as a 'slow-blue nuclear hypervariable': a galaxy with no previously known active nucleus, blue colours, and large-amplitude brightness evolution occurring on a time-scale of years. Subsequent observations have shown that this source does indeed contain an active galactic nucleus (AGN). Our optical photometric and spectroscopic monitoring campaign has recorded one major dimming event (and subsequent rise) over a period of around 4 yr; there is also evidence of previous events consistent with this in archival data recorded over the last 20 yr. Here we report an analysis of the 11 optical spectra obtained to date and we assemble a multiwavelength data set including infrared, ultraviolet, and X-ray observations. We find that an intrinsic change in the luminosity is the most favoured explanation of the observations, based on a comparison of continuum and line variability and the apparent lagged response of the hot dust. This source, along with several other recently discovered 'changing-look' objects, demonstrate that AGNs can exhibit large-amplitude luminosity changes on time-scales much shorter than those predicted by standard thin accretion disc models.

Key words: accretion, accretion discs – black hole physics – galaxies: active – galaxies: individual: SDSS J223210.52−080621.3 – quasars: emission lines.

1 INTRODUCTION

Active galactic nuclei (AGNs) are powered by the gravitational energy reprocessed as matter spirals inward and is finally accreted by the central supermassive black hole (BH). Two of the defining characteristics of AGNs are their very high bolometric luminosities, and in the case of those that are not obscured, by their significant multifrequency variability on many time-scales. Numerous variability studies have been conducted, both on large samples of AGNs (e.g. Stripe 82, MacLeod et al. 2012; Schmidt et al. 2012; Zuo et al. 2012) and detailed studies of individual cases (e.g. NGC 4593 by McHardy et al. 2018 and NGC 5548 by Pei et al. 2017 and references therein). In addition to these studies some cases of extreme variability have been identified in the form of the so-called 'changing-look' quasars (CLQs; e.g. LaMassa et al. 2015; MacLeod et al. 2018; Rumbaugh et al. 2018; Yang et al. 2018) which are AGNs with (dis)appearing broad emission lines as well as strong continuum changes. It is very probable that more than one physical mechanism is responsible for the variations seen across all samples. Changes in the dust extinction in some AGNs were proposed in early studies (e.g. Goodrich 1995), but this explanation is not generally preferred in the case of changing-look AGN. In recent studies, often the most favoured cause is a change in the emission from the accretion disc or its associated Comptonization regions (e.g. LaMassa et al. 2015; MacLeod et al. 2016; Parker et al. 2016; Ruan et al. 2016; Runnoe et al. 2016; Gezari et al. 2017; Sheng et al. 2017; Katebi et al. 2018; Noda & Done 2018; Ross et al. 2018; Stern et al. 2018; Wang, Xu & Wei 2018). Other, rarer events, such as stellar tidal disruption, supernovae in the nuclear regions, and gravitational microlensing, have also been proposed (e.g. Lawrence et al. 2016; Bruce et al. 2017 and references therein). To make further progress it is important to better characterize the properties of variability to help distinguish between the various mechanisms responsible.

1.1 The source SDSS J2232−0806

SDSS J223210.51−080621.3 (hereafter SDSS J2232−0806) is an AGN at redshift $z = 0.276$ (Collinson et al. 2018). It was identified as a 'slow-blue nuclear hypervariable' object by Lawrence et al. (2016) on the basis that it showed large-amplitude optical brightness variability ($|\Delta g| \geq 1.5$) and the change was slow and blue (occurring

★ E-mail: daniel.kynoch@durham.ac.uk

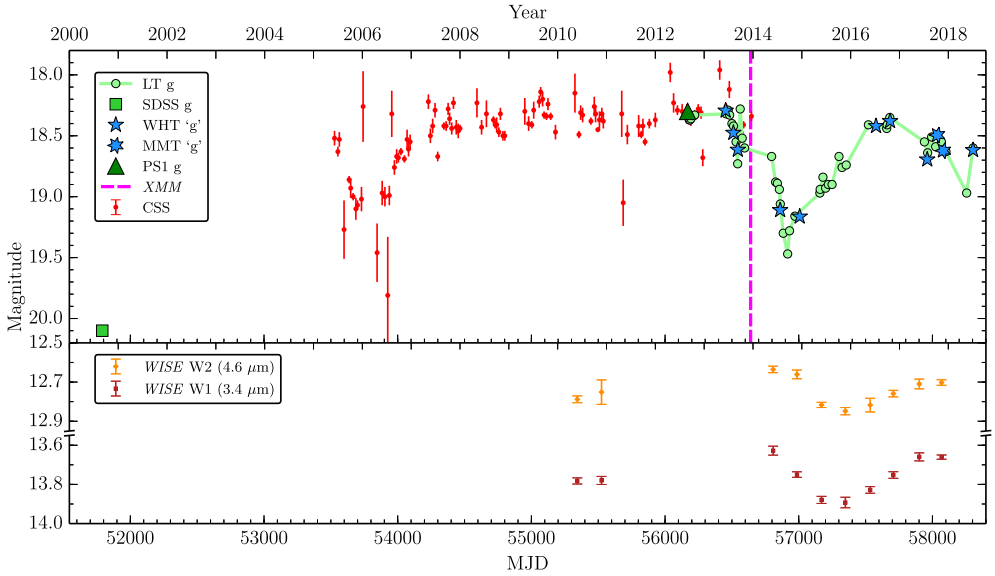

Figure 1. *Top*: the optical light curve of SDSS J2232−0806. The source was observed to brighten by $\Delta g = 1.8$ mag between the SDSS observation made in 2000 and the PS1 observation of 2012. We show our follow-up optical photometric monitoring with the LT and archival data from the Catalina Sky Survey (CSS). As well as the direct photometric points, we show the equivalent g magnitudes derived from spectroscopic observations made with the WHT and the MMT. A global grey-scale flux correction of −0.15 mag has been applied to the spectral magnitudes (see Section 2.2 in the text). The date of our *XMM–Newton* X-ray and optical-UV observations is also indicated. *Bottom*: the *WISE* infrared light curves of SDSS J2232−0806 (see Section 3.2.1 in the text).

over several years, in contrast to the fast and red transients which are likely associated with supernovae).

Our photometric monitoring of this source with the Liverpool Telescope (LT) since 2013 has captured one substantial dimming event, and there is sparsely sampled archival photometry that is consistent with similar past events.

1.2 The aims of this study

We aim to investigate whether the variability behaviour of this source is best explained by either obscuration of the nucleus, or by some intrinsic change in the emission from the central engine. The optical spectroscopic monitoring campaign conducted with the William Herschel Telescope (WHT) allows us to investigate changes in both the AGN continuum and line emission from the broad-line region (BLR).

Throughout this paper, we assume a flat ΛCDM cosmology with $H_0 = 70\,\mathrm{km\ s^{-1}\ Mpc^{-1}}$, $\Omega_\mathrm{m} = 0.3$, and $\Omega_\Lambda = 0.7$. For the redshift $z = 0.276$ this cosmology implies a luminosity distance of 1410.8 Mpc and a flux-to-luminosity conversion factor of $2.38 \times 10^{56}\ \mathrm{cm^2}$.

2 THE OPTICAL MONITORING CAMPAIGN

Lawrence et al. (2016) found that in 2012 the PanSTARRS-1 (PS1) 3π Survey g-band photometry of SDSS J2232−0806 was 1.8 mag brighter than it was in a Sloan Digital Sky Survey (SDSS) photometric observation made in 2000. To further investigate this interesting source, a photometric monitoring campaign began in 2012 using the LT and is ongoing. Optical spectroscopic monitoring commenced in 2013, primarily using the WHT, with an additional two spectra taken in late 2017 with the MMT. The observing campaign has revealed a dip in brightness of around a factor of 3 in flux and shows a recovery in our most recent observations. In this section we present our analysis of the optical data.

2.1 Observations and data reduction

2.1.1 Liverpool Telescope optical photometric monitoring

The LT is a fully robotic, remotely controlled 2 m telescope that observes autonomously from La Palma in the Canary Islands. Photometric observations were taken in the r, g, and u bands. 44 independent photometric observations obtained using the g filter ($\lambda_\mathrm{eff} = 4696$ Å) between 2012 September and 2018 July are shown in Fig. 1. The g and r bands are much more frequently sampled than the u band, for which we have only 21 photometry points. The observed variability amplitude in the g band ($\Delta g \approx 1.2$) is greater than that of r band ($\Delta r \approx 0.8$) although we note that the r band ($\lambda_\mathrm{eff} = 6111$ Å) is subject to increasing contamination from the host galaxy as the AGN contribution diminishes. In addition, the u band ($\lambda_\mathrm{eff} = 3499$ Å) covers the strong, broad Mg II emission line (observed at 3573 Å) and so it is not a clean measure of the AGN continuum. For these reasons, in this study we use only photometry obtained in the g band.

2.1.2 William Herschel Telescope optical spectroscopic monitoring

The 4.2 m WHT is also situated on the island of La Palma. SDSS J2232−0806 has been observed with the WHT on nine occasions between 2013 June and 2018 July. We used the Intermediate dispersion Spectrograph and Imaging System (ISIS) long-slit, double spectrograph with the 5300 Å dichroic which directed the light into the red and blue arms containing the R158B and R300B gratings, respectively. Typically ×2 binning in the spatial direction was used to improve the signal-to-noise ratio (SNR). This set-up gave a spectral resolution of $R \approx 1000$ at 7200 Å in the red and $R \approx 1500$ at 5200 Å in the blue, for a slit width of 1 arcsec. The total wavelength coverage was ≈3100–10600 Å, this window includes the principal emission lines Mg II λ2800, Hβ λ4861, [O III] λλ4959, 5007, and Hα λ6563.

The data reduction was performed with a pipeline using custom PYRAF scripts and standard techniques. The pipeline is described in detail in Bruce et al. (2017, section 2.3.3 in that paper).

Unfortunately, we do not have a spectrum contemporaneous with the nadir of the LT light curve, which occurred around 2014 September 17. The spectra obtained on 2014 July 23 and December 16 were recorded 56 d before and 90 d after the photometric minimum and sample the falling and rising side of the dip in the light curve, respectively (see Fig. 1).

2.1.3 MMT spectroscopic monitoring

The MMT is a single 6.5 m mirror telescope on Mount Hopkins, Arizona. Two optical spectra of SDSS J2232−0806 were obtained in 2017 December. The observations were conducted during grey time; on both occasions the observing conditions were clear with subarcsecond seeing. We used the MMT Blue Channel spectrograph with the 300 g mm^{-1} grating and a 1 arcsec slit. This set-up gives a spectral resolution of $R \approx 740$ at 4800 Å, lower than that we obtained with the WHT. The target spectra that we use here are the coadded medians of three 10 min exposures.

2.2 Optical spectral analysis

Optical and ultraviolet fluxes are affected by reddening caused by dust in the Milky Way. The Galactic neutral hydrogen column density towards SDSS J2232−0806, $N_{\rm H} = 4.52 \times 10^{20}$ cm^{-2} (Dickey & Lockman 1990), implies a colour excess $E(B-V) = 0.078$ mag based on the relation derived by Bohlin, Savage & Drake (1978). Here, and in Section 3, we correct our data for Galactic reddening using this value of $E(B-V)$ and the Milky Way reddening curve of Cardelli, Clayton & Mathis (1989).

2.2.1 Internal scaling of spectra

Before we perform our spectral analysis, we rescale our spectra to account for variations in the absolute flux calibration caused by effects such as seeing (slit losses) and thin cloud. Since the strong, narrow [O III] λ5007 forbidden emission line originates in a low-density, large-volume gas, it should not vary during the course of our monitoring period and is therefore a suitable line to use for internal cross-calibration (provided it is not spatially resolved). Rather than simply assuming the flux in the line remains constant (which depends upon an accurate determination of the underlying continuum flux level), we assume instead that the line profile is constant and determine the appropriate flux scaling factors using the PYTHON package MAPSPEC developed by Fausnaugh (2017). This package is an implementation of, and improvement on, the method of van Groningen & Wanders (1992). As noted by them this method should produce a more accurate internal flux scaling than the standard method of simply scaling each spectrum so that the integrated [O III] λ5007 line flux is equal to a chosen reference value.

2.2.2 Absolute flux scaling of spectra

From our internally scaled optical spectra, we calculated the equivalent LT g magnitude. The LT optical CCD camera was changed from the RATcam to the IO:O at the end of 2014 February, so in our calculations we use the filter specifications appropriate to the LT instruments in use at the time the spectrum was recorded, although the resultant difference in magnitude is very minor. For each spectrum we measured the mean flux $\langle \nu F_\nu, g \rangle$ in the LT g band (RATcam 3945–5532 Å, IO:O 3933–5630 Å) then calculated the g magnitude equivalent

$$g = -2.5 \log \left(\frac{\langle \nu F_\nu, g \rangle \times 10^{23}}{\nu_{\rm eff}\ {\rm ZP}} \right) \ {\rm mag}, \quad (1)$$

where ZP is the zero-point magnitude of the filter (RATcam 3940.5 Jy; IO:O 3936.7 Jy) and $\nu_{\rm eff}$ is the frequency equivalent to the filter's effective wavelength $\lambda_{\rm eff}$ (RATcam 4730 Å; IO:O 4696 Å).

By comparison with the LT g magnitudes, we found that the equivalent magnitudes appeared systematically offset by ≈0.15 mag. This slight discrepancy is likely due to slit losses, resulting in a lower flux in our narrow-slit spectra compared with the large-aperture photometry. Adjusting the magnitudes by −0.15 mag (an increase of ≈15 per cent in flux) the equivalent magnitudes replicate both the shape and level of the LT light curve, as can be seen in Fig. 1. In the following, all of the measurements that we make from the spectra include the internal and absolute flux scalings described here.

2.2.3 Comparison of the optical spectra

All 11 optical spectra are shown in the top panel of Fig. 2. To highlight the spectral variability we have coloured the brightest and faintest spectra in blue and red, respectively, and plotted both their difference and ratio in green and purple, respectively, in the panels below. The ratio between the brightest and faintest spectrum shows the fractional variability at each wavelength. The fractional variability at longer wavelengths is diluted by emission from the host galaxy and we see in the ratio spectrum that the fractional variability is greater in the blue end. Taking the difference removes the constant components including the host galaxy. In the difference spectrum it can be seen that the absolute flux variation in the blue continuum ($\lambda \lesssim 4200$ Å) is greater than in the red. The [O III] λλ4959, 5007 lines, which we assumed to be non-variable, are absent in the difference spectrum which gives us confidence that the flux scaling method we have adopted works well. Whereas differences in the Hα and Hβ lines between bright and faint spectra are clear, the Mg II line appears to be less variable. This is obvious in the ratios of the continuum-subtracted lines (shown in purple in the lower panels of the bottom three plots of Fig. 2) where the core of Mg II changes very little and no substantial change is apparent in the broad wings. The change in the Balmer lines is most apparent on the blue side of the lines, which seem to have a slight 'red shoulder' in the fainter spectra. A similar skewness of the Hα profile in the faint state of the CLQ J0159+0033 was found by LaMassa et al. (2015).

We computed the mean and root-mean-square (rms) spectra following the method of Peterson et al. (2004). Before performing the calculations, the single-epoch spectra are first shifted in wavelength so that the centroids of the [O III] λ5007 lines (as determined from our model fits) are aligned. The two MMT spectra are noisier than the nine obtained at the WHT and have less wavelength coverage (particularly redward of Hα). We confirmed that the shapes and general features of our mean and rms spectra are (broadly) unchanged if we exclude the MMT spectra. Having done so, we proceeded with the mean and rms spectra determined from just the WHT observations, so as to extend our results into the red.

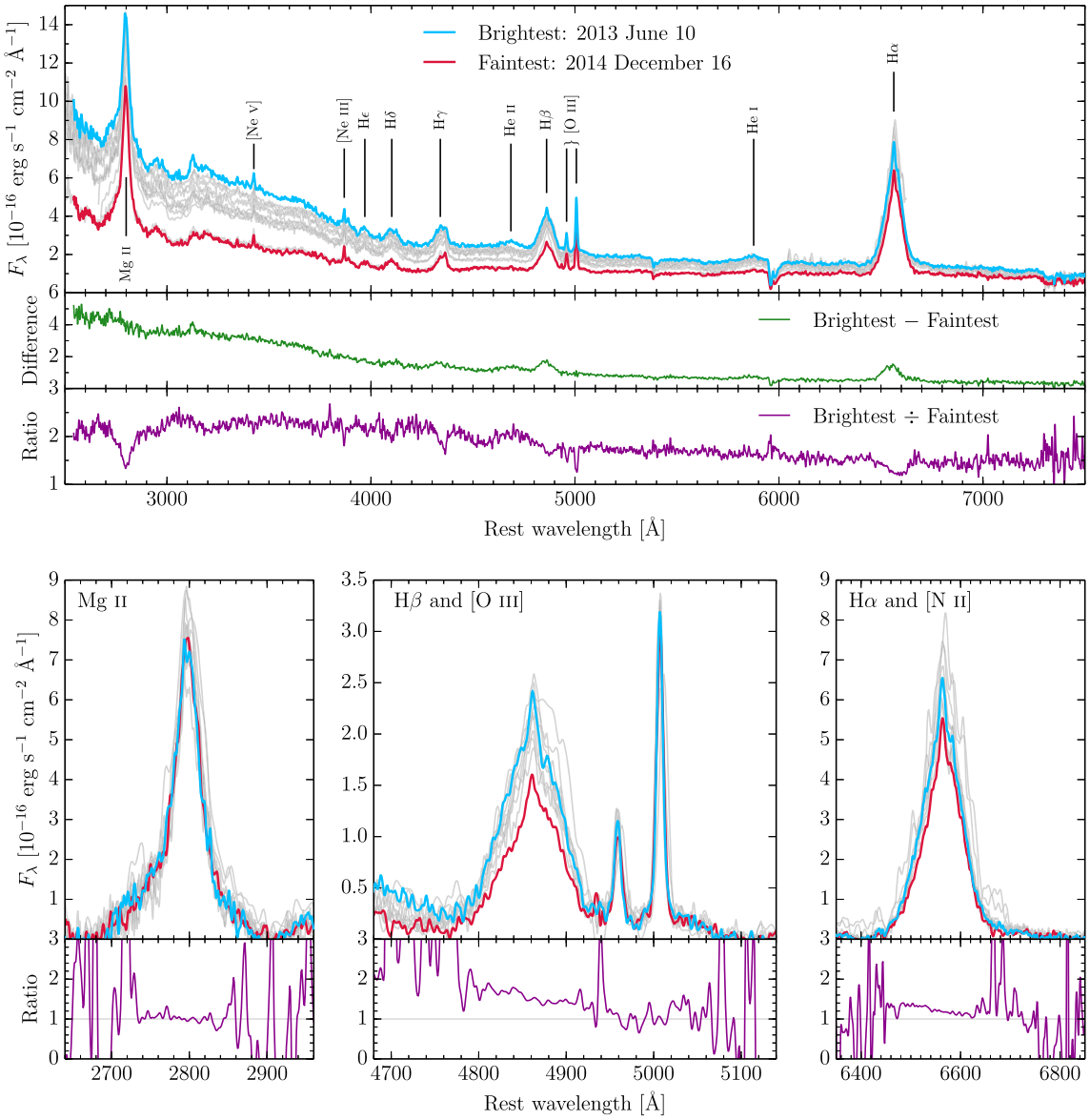

Figure 2. *Top*: All 11 optical spectra of SDSS J2232−0806, rescaled to the same [O III] λ5007 emission line profile and corrected for Galactic reddening ($A_V = 0.24$). The brightest spectrum (2013 June) is shown in blue and the faintest spectrum (2014 December) is shown in red; the other nine spectra are shown in grey. Prominent emission lines are labelled. In the lower panels the difference spectrum is shown in green and the ratio spectrum in purple. *Bottom*: Continuum-subtracted regions containing key emission lines. Spectra are colour coded as in the top plot. In the lower panels, the ratios between the brightest and faintest spectra are shown in purple.

The resultant spectra are shown in Fig. 3. As in the difference spectrum, the [O III] lines are removed in the rms spectrum whereas the Balmer lines, Balmer continuum (≈2000–4000 Å), and He II λ4685 are all visible. We also note that the Mg II emission line is absent from the rms spectrum, which we discuss later. Comparing the shapes of the mean and rms spectra, we see that the rms spectrum is bluer since the non-variable host galaxy component has been removed: we discuss this in Section 3.3.1. The shape of the rms spectrum is very similar to that of an accretion disc; in Fig. 3 we show a standard disc spectrum for comparison, calculated for a BH mass of 2×10^8 $M_\odot$, $L/L_{\rm Edd} = 0.03$ and outer radius of 100 gravitational radii (equal to that determined in our spectral energy distribution (SED) model in Section 3.3.2).

2.3 Measurement of the continuum and the emission lines

The continuum and emission line fitting was performed using a custom PYTHON script employing the LMFIT package[1] which employs a Levenberg–Marquardt algorithm for non-linear, least-squares minimization. The fitting routine appeared to underestimate the errors on the returned parameters, so rather than quoting the error on a single fit, an iterative approach was taken. Each spectrum was fitted 100 times: on each iteration Gaussian noise was added to the flux density with the amplitude of the noise determined by the measurement error. The final model parameters

[1] https://lmfit.github.io/lmfit-py/

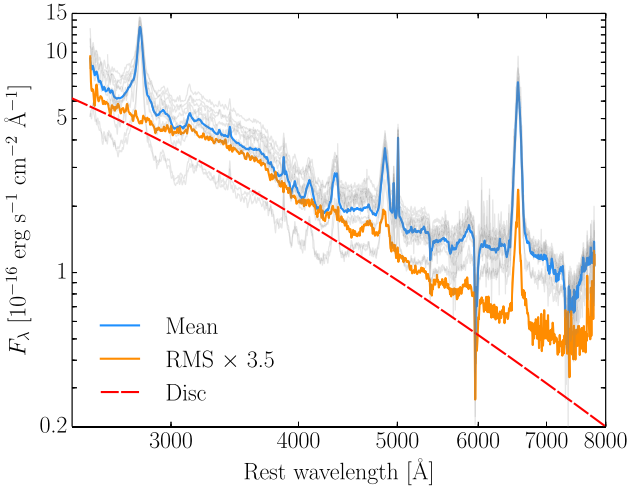

Figure 3. The mean spectrum of SDSS J2232−0806 is shown in blue and the rms spectrum is shown in orange. The rms spectrum has been scaled up by a factor of 3.5 to ease the comparison with the mean. The 11 spectra from the monitoring campaign are underplotted in grey. The dashed red line shows the model spectrum of an AGN accretion disc with $L/L_{\rm Edd}$ = 3 per cent and $R_{\rm out} = 100\,R_{\rm g}$.

and errors are the mean and standard deviation calculated from the 100 iterations. The standard deviation quantifies the spread of parameter values that can reasonably fit the data. The errors on the physical quantities derived from the model parameters (e.g. the line flux, equivalent width etc.) have been propagated using standard methods. The results of our iterative fitting procedure are tabulated in Tables A1, A2, and A3 in the Appendix.

2.3.1 *Red continuum determination*

For the WHT spectra, the (rest frame) 3900–7800 Å continuum is estimated from five emission line free windows of width 50 Å; these are centred on the wavelengths 4240, 5100, 6205, 7050, and 7700 Å. Because of the narrower wavelength coverage of the two spectra obtained using the MMT, only the first three of these windows are available. We fit a power-law continuum of the form $F_\lambda = C\,(\lambda/5100\,\text{Å})^{-\alpha}$ through these points to determine the global continuum, allowing the slope α and normalization C to be free parameters in the fit.

2.3.2 *Modelling of the principal emission lines*

To model the Balmer lines, the red continuum is subtracted from two wavelength windows containing the emission lines of interest (rest frame 4740–5100 Å for Hβ and [O III]; 6380–6800 Å for Hα and [N II]). The permitted lines were initially fit with a sum of two Gaussians (one broad and one narrow) with the same central wavelength. However, there were clearly substantial residuals in the line profiles, particularly prominent in the red wing of Hα. We therefore added a third Gaussian component to the Balmer lines, modelling a very broad base, and allowed this to be offset from the central wavelength of the narrower components. The two [N II] forbidden lines were each fit with a single, narrow Gaussian. As well as a strong, narrow Gaussian, a weak, broad Gaussian base was added to the [O III] λ4959 and λ5007 lines. In all fits we include the permitted Fe II emission line template of Bruhweiler & Verner (2008), with its normalization left as a free parameter in the fits. The model was refined to include the following constraints:

(i) all narrow, broad, and very broad lines have the same velocity width (with the exception of the broad bases of the [O III] forbidden lines: these had equal width but this was not tied to the width of the broad permitted lines);
(ii) the very broad lines in the Hα and Hβ profiles have the same velocity offset;
(iii) it proved impossible to reliably fit both the width and offset of the very broad lines simultaneously so we fixed the velocity width of these components to ≈11500 km s^{-1} and placed the limit $\Delta v_{\rm vb} \lesssim +2500$ km s^{-1} on the offset;[2]
(iv) the [O III] λ4959 and λ5007 lines have a fixed flux ratio of 1:3;
(v) the [N II] λ6548 and λ6583 lines have a fixed ratio of 1:3;
(vi) the stronger [N II] λ6583 line has its amplitude fixed to the mean value determined in the WHT spectra;
(vii) the narrow lines ought not to vary significantly over the monitoring period, therefore the Hα narrow line was fixed to 0.67 of the [O III] λ5007 flux, the error-weighted mean value determined from all of the WHT spectra;
(viii) the Balmer decrement of the narrow lines was a challenge to determine so was fixed at 6.7, again the error-weighted mean value determined from the WHT spectra.

The narrow-line Balmer decrement adopted here is high, although it is within the range ≈1–12 found by Jin et al. (2012) for a sample of 51 type 1 AGN and at the upper end of the range found by Lu et al. (2019) for 554 SDSS DR7 quasars. If the intrinsic narrow-line region (NLR) Balmer decrement is 2.9 (Osterbrock & Ferland 2006) the measured value implies an NLR reddening of $A_V \approx 2.6$ mag. However, our aim is to investigate relative changes in the broad-line decrement so as long as the subtraction of the narrow-line components is consistent, its precise value will have little effect on our results.

In calculating the Balmer and [O III] emission line equivalent widths (EWs) we have subtracted the host galaxy contribution to the flux beneath the line (these are determined in Section 3.3.1) so that the strength of the line is assessed relative to the AGN continuum emission alone.[3] The Balmer, [O III], and [N II] line properties derived from the best-fitting model parameters are quoted in Tables A1 and A2. Examples of our Balmer, [O III], and Mg II emission line fits are shown in Fig. 4.

Since there are no emission line free regions in the vicinity of the Mg II line, we do not subtract the continuum before fitting the line. Instead we fit the line, Fe II template and a power-law continuum simultaneously in the wavelength window 2650–2950 Å. The Mg II λλ2795, 2802 doublet was not resolved in the composite spectrum produced by stacking the WHT spectra; we therefore fit a single Mg II λ2800 profile. This emission line was fitted with two Gaussians, one broad and one very broad for the base. As well as measuring the full width at half-maximum (FWHM) of the two components separately, we also calculate the FWHM of the total line profile. The quantities derived from the best-fitting model parameters are quoted in Table A3.

[2]The line width is approximately equal to the mean FWHM of the very broad Balmer line components of the broad-line AGN modelled by Jin, Ward & Done (2012). The offset was limited to keep the centre of the very broad component within the core of the line.
[3]The host galaxy makes a negligible contribution at the wavelength of Mg II.

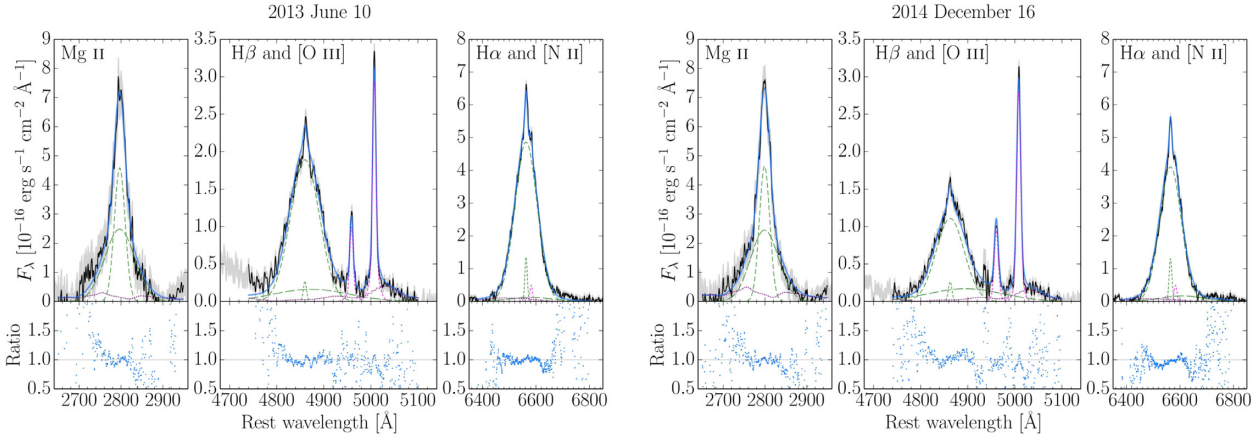

Figure 4. Examples of emission line fits to continuum-subtracted spectral windows. In the upper panels, the solid black lines show the wavelength regions of the spectra that were fit, and the solid grey area indicates the error on the flux density; the green short-dashed, dashed, and long-dashed lines show the modelled narrow, broad, and very broad components of the permitted lines, respectively; the magenta short-dashed lines show the modelled [O III] and [N II] forbidden lines; an Fe II emission template is shown by the purple dotted line and the total model is shown by the solid blue line. The lower panels show the data / model ratios in the fitted regions.

Table 1. BH mass estimates from optical spectra.

Relation	log (*K*)	α	FWHM	*L*	$M_{\rm BH}$
FWHM (Hα), $\lambda L_{5100\,\text{Å}}$	6.845	0.650	4.51	1.66	2.0
FWHM (Hα), $L_{\rm H\alpha}$	7.389	0.563	4.51	0.13	1.6
FWHM (Hβ), $\lambda L_{5100\,\text{Å}}$	6.740	0.650	4.51	1.66	1.6
FWHM (Mg II), $\lambda L_{3000\,\text{Å}}$	6.925	0.609	4.19	4.21	3.5

The broad line FWHMs are in 10^3 km s^{-1}, the luminosities *L* in 10^{44} erg s^{-1}, and the calculated BH masses $M_{\rm BH} = KL^\alpha \times \text{FWHM}^2$ in 10^8 M$_\odot$.

2.4 The black hole mass

To calculate the mass of the BH from our emission line and continuum measurements we use the relation

$$M_{\rm BH} = K \times L^\alpha \times \text{FWHM}^2 \quad (2)$$

of Mejía-Restrepo et al. (2016) with the appropriate values of *K* and α taken from their table 7 (the local calibration corrected for small systematic offsets) for the relevant combinations of the emission line FWHM and continuum or line luminosity *L*. In Table 1 we quote the *K* and α values used for each relation along with the line and continuum parameters determined as the error-weighted means of values obtained in the four brightest spectra.[4] We find that the mass is in the range $M_{\rm BH} = 1.6$–3.5×10^8 M$_\odot$ (see Table 1), marginally greater than the 1.2–1.6×10^8 M$_\odot$ determined by Collinson et al. (2018). There are considerable uncertainties on the masses estimated by virial methods, which are due to the scatter on the scaling relations. For relations based on Hα and Hβ the 1σ scatter is in the range 0.13–0.18 dex; the Mg II relation has a greater scatter of 0.25 dex. We adopt a mass of 2×10^8 M$_\odot$ in the following.

3 MULTIWAVELENGTH DATA

3.1 X-ray and UV observation with *XMM–Newton*

A 30 ks *XMM–Newton* observation of SDSS J2232−0806 was made on 2013 December 14 (OBS ID: 0724441001; PI: Lawrence). At this time, the source was in a relatively high optical flux state (see Fig. 1). The three EPIC X-ray detectors (pn, MOS1, and MOS2) were operating in a Full Frame mode with the Thin filter in place. Ultraviolet photometry was recorded by the onboard Optical Monitor (OM) which cycled through three of the six filters: U, UVW1, and UVM2.

The data were reduced using the *XMM* Science Analysis Software (SAS, v16.0.0) and the latest calibration files available at the time. The X-ray observation suffered from substantial particle background flaring such that, after filtering, the remaining good time intervals were 8.6, 8.5, and 8.2 ks for the pn, MOS1, and MOS2 detectors, respectively. The source spectra were extracted from 47 arcsec radius circular regions centred on the source. The background spectrum was extracted from larger 94 arcsec radius circular regions offset from the source on a blank area of sky. The spectra were regrouped so as not to oversample the detectors' intrinsic energy resolution by a factor of more than 3 and to contain at least 20 counts per energy bin, so that they are suitable for a χ^2 analysis.

The OM photometry in the three filters were extracted using the SAS tasks OMICHAIN and OMISOURCE, following the standard procedures. The OM filter bandpasses cover several emission lines and so do not accurately represent the continuum flux level. Following the method of Elvis et al. (2012), we can 'correct' the photometric fluxes to obtain an improved estimate of the continuum level by multiplying the measured fluxes by the photometric correction factor

$$P_{\rm c} = \frac{\text{BW}}{\text{EW}_{\rm rest} \times (1+z) + \text{BW}} \quad (3)$$

where BW is the bandwidth of the photometric filter covering a line of rest-frame equivalent width, $\text{EW}_{\rm rest}$. The OM U filter (BW = 840 Å) covers the Mg II emission line, for which we estimate $\text{EW}_{\rm rest} \approx 60$ Å $\rightarrow P_{\rm c} = 0.92$. Assuming a C III] $\text{EW}_{\rm rest} \approx 24$ Å (Vanden Berk et al. 2001), the correction factor in the UVM2 filter is $P_{\rm c} = 0.95$. We conclude that the UVW1 filter is very weakly affected by line emission, since the C III] and Mg II lines only partially appear at the very ends of its bandpass where the sensitivities are lowest.

[4]Those recorded on 2013 June 10 and August 7 and 2016 July 9 and October 22.

Table 2. X-ray spectral models.

Model	Parameter	Value
POWERLAW	Γ	2.19 ± 0.02
	Norm.	$(2.83 \pm 0.04) \times 10^{-4}$
	χ^2/d.o.f.	$223/175 = 1.27$
BKNPOWER	Γ_1	$2.35^{+0.04}_{-0.05}$
	$E_{\rm brk}$ (keV)	$1.7^{+0.5}_{-0.2}$
	Γ_2	$1.79^{+0.07}_{-0.17}$
	Norm.	$\left(2.71^{+0.07}_{-0.05}\right) \times 10^{-4}$
	χ^2/d.o.f.	$175/173 = 1.01$
ZPHABS ×	$N_{\rm H}^{\rm int}$ (10^{19} cm^{-2})	<7
BKNPOWER	Γ_1	$2.35^{+0.04}_{-0.02}$
	$E_{\rm brk}$ (keV)	$1.7^{+0.5}_{-0.2}$
	Γ_2	$1.79^{+0.07}_{-0.20}$
	Norm.	$\left(2.71^{+0.06}_{-0.05}\right) \times 10^{-4}$
	χ^2/d.o.f.	$175/172 = 1.01$

All models included a Galactic absorption component (PHABS) with the column density fixed at $N_{\rm H}^{\rm Gal} = 4.52 \times 10^{20}$ cm^{-2}.

3.1.1 X-ray spectral analysis

Analysis of the X-ray spectra was performed in XSPEC (Arnaud 1996) v12.9.1e. The spectra from the three EPIC detectors were fitted simultaneously, allowing for cross-normalization factors to account for differences in calibration between the detectors; these did not vary by more than 5 per cent. All models included a Galactic absorption component (PHABS) with the column density fixed at $N_{\rm H}^{\rm Gal} = 4.52 \times 10^{20}$ cm^{-2}. A single power law was an unsatisfactory fit to the data, giving a reduced χ^2 of 1.27. A broken power law was a significant improvement, decreasing the χ^2 value by 48 for the introduction of two additional free parameters and we achieve an acceptable fit with a reduced χ^2 of 1.01. The *F*-test probability of this improved model was >99.99 per cent. We then tested for an intrinsic absorber by the inclusion of a ZPHABS component with the redshift fixed to that of the source. This gave no significant improvement in the fit and we determined an upper limit on the intrinsic column density $N_{\rm H}^{\rm int} < 7 \times 10^{19}$ cm^{-2}. The X-ray spectral model parameters are given in Table 2.

3.2 Archival photometric data

3.2.1 WISE

The *Wide-field Infrared Survey Explorer* (*WISE*; Wright et al. 2010) telescope observed SDSS J2232−0806 twice in 2010. Data for this source was found in the AllWISE Source Catalogue, hosted by the Infrared Science Archive (IRSA[5]); in Table 3 we quote the reported instrumental profile-fit magnitudes. The photometric quality of these detections were A (best) for the W1, W2, and W3 filters and B for the W4 filter.

As well as the catalogue magnitudes, we also obtained infrared light curves in the W1 and W2 filters from the *WISE* and *Near-Earth Orbit WISE Reactivation* (*NEOWISE*) archives.[6] In addition to the two visits made during the *WISE* mission, SDSS J2232−0806 has been observed with roughly 6-month cadence since the start of *NEOWISE* mission in 2013 December. Typically a dozen exposures are made on each visit; to construct the light curves shown in Fig. 1, we have calculated the mean and standard error on the magnitudes recorded on each visit. We exclude the seven exposures taken on MJD 57345, because there was a large scatter on these magnitudes and a set of 11 exposures was taken 3 d later. This visit on MJD 57348 (2015 November 19) corresponds to the minima of the infrared light curves and occurs 428 d later than the observed minimum in the LT optical light curve (see Section 2.1.1). There is a 0.26 mag peak-to-trough change in W1 and a 0.21 mag change in W2.

3.2.2 Two-Micron All Sky Survey

SDSS J2232−0806 was observed as part of the Two-Micron All Sky Survey (2MASS; Skrutskie et al. 2006), which was conducted between 1997 and 2001. In Table 3 we quote the *J*, *H*, and K_s profile-fit magnitudes reported in the 2MASS All-Sky Point Source Catalog (PSC).[7] The observation was made on 1998 October 1 and the photometric quality flag is C for all filters.

3.2.3 Sloan Digital Sky Survey

Although no SDSS spectroscopic data exists for this source, photometry was obtained on 2000 March 9. As can been seen in Fig. 1, the source was in a very low state at this time. The object was classified as a (passive) galaxy based on its photometric colours.

3.2.4 PanSTARRS-1 3π Survey

The PS1 3π Survey was conducted between 2009 and 2014, observing the 3/4 of the sky north of −30° declination multiple times per year in each of five filters (see Magnier et al. 2013; Chambers et al. 2016). Originally searching for tidal disruption events, Lawrence et al. (2016) identified SDSS J2232−0806[8] as one of a number of 'slow blue nuclear hypervariables': objects with no previously known AGN, blue colours, and evolution on time-scales of years. This particular source was brighter by $\Delta g = 1.80 \pm 0.04$ in 2012 compared with the SDSS photometry of 2000.

3.2.5 UK Schmidt Telescope

We located a record for SDSS J2232−0806 in the SuperCOSMOS Science Archive (SSA[9]). The B_j band ($\lambda = 3950$ Å) observation was made using the UK Schmidt Telescope (Cannon 1975) on Siding Spring Mountain, NSW, Australia, on 1986 August 1. Its sCorMag (stellar magnitude in the Vega system) is given in the SSA as $B_j = 19.02$ mag. Converting this to a *g* band AB magnitude, we estimate $g \approx 18.6 \pm 0.3$, where the uncertainty is the standard single-passband uncertainty on SuperCOSMOS magnitudes (Hambly et al. 2001).

3.2.6 Hubble Space Telescope

Two short-exposure photometric observations were made with the Wide Field Camera 3 (WFC3) onboard the *Hubble Space Telescope* (*HST*) on 2015 September 18. The exposure times were 330 s in the

[5] http://irsa.ipac.caltech.edu/.
[6] Because of the depletion of hydrogen coolant, only the W1 and W2 filters have been operable since the beginning of the *NEOWISE* mission.
[7] Also available from IRSA, see earlier note.
[8] The common name of the source in this paper is J223210.
[9] http://ssa.roe.ac.uk/.

Table 3. The multiwavelength photometric data set.

Date	Telescope or survey	Filter	Measurement	Unit	log (ν)[b]	Flux[c]	Luminosity[d]
2010-05-27–28	*WISE*	W4	7.536 ± 0.157	Vega mag	13.13	1.10 ± 0.16	2.62 ± 0.38
2010-05-27–28	*WISE*	W3	10.258 ± 0.073	Vega mag	13.41	6.48 ± 0.44	15.4 ± 1.0
2010-05-27–11-25	*WISE*	W2	12.783 ± 0.027	Vega mag	13.81	8.62 ± 0.21	20.5 ± 0.5
2010-05-27–11-25	*WISE*	W1	13.782 ± 0.027	Vega mag	13.95	8.50 ± 0.21	20.2 ± 0.5
1998-10-01	2MASS	K_s	15.419 ± 0.182	mag	14.14	6.29 ± 1.06	15.0 ± 2.5
1998-10-01	2MASS	H	16.166 ± 0.208	mag	14.26	6.31 ± 1.21	15.0 ± 2.9
1998-10-01	2MASS	J	17.124 ± 0.201	mag	14.39	5.47 ± 1.01	13.0 ± 2.4
2000-03-09	SDSS	z	18.33 ± 0.04	asinh mag	14.53	5.6 ± 0.2	14.8 ± 0.5
2000-03-09	SDSS	i	18.97 ± 0.02	asinh mag	14.61	3.78 ± 0.07	10.4 ± 0.2
2000-03-09	SDSS	r	19.20 ± 0.02	asinh mag	14.69	3.71 ± 0.07	10.8 ± 0.2
2000-03-09	SDSS	g	20.10 ± 0.03	asinh mag	14.81	2.14 ± 0.06	6.7 ± 0.2
2012-08-30	PanSTARRS-1 3π	g	18.30 ± 0.05	mag	14.80	11.0 ± 0.5	34 ± 2
2012-09-11	Liverpool	g	18.37 ± 0.02	AB mag	14.81	10.5 ± 0.2	33.0 ± 0.6
1988-06-01	Schmidt	g^a	18.6 ± 0.3	AB mag	14.81	9 ± 2	27 ± 6
1988-06-01	Schmidt	B_j	19.0 ± 0.3	Vega mag	14.88	10 ± 3	33 ± 7
2000-03-09	SDSS	u	19.79 ± 0.05	asinh mag	14.92	3.8 ± 0.2	12.7 ± 0.7
2013-12-14	*XMM–Newton* OM	U	2.219 ± 0.038	cts s^{-1}	14.94	14.8 ± 0.2	50.4 ± 0.7
2013-12-14	*XMM–Newton* OM	UVW1	1.154 ± 0.017	cts s^{-1}	15.01	16.2 ± 0.2	58.5 ± 0.7
2013-12-14	*XMM–Newton* OM	UVM2	0.390 ± 0.011	cts s^{-1}	15.11	19.9 ± 0.6	89 ± 3
2003-08-22	*GALEX*	NUV	20.67 ± 0.22	AB mag	15.12	2.6 ± 0.5	12 ± 2
2004-08-24	*GALEX*	NUV	19.81 ± 0.04	AB mag	15.12	6.8 ± 0.2	31 ± 1
2003-08-22	*GALEX*	FUV	21.10 ± 0.32	AB mag	15.29	2.6 ± 0.7	11 ± 3
2004-08-24	*GALEX*	FUV	19.62 ± 0.03	AB mag	15.29	8.4 ± 0.3	36 ± 1

Notes. [a]Converted from the quoted B_j magnitude below.
[b]Logarithm of the observed frequency ν in Hz;
[c]observed flux νF_ν in units of 10^{-13} erg s^{-1} cm^{-2};
[d]intrinsic luminosity νL_ν in units of 10^{43} erg s^{-1}, dereddened where appropriate.

wide IR F125W filter ($\lambda_{\rm eff} = 1.25$ μm, J band) and 1200 s in the extremely wide UVIS F475X filter ($\lambda_{\rm eff} \approx 4776$ Å, and including the g band).

3.2.7 GALEX

Two epochs of ultraviolet (UV) photometry were found by searching the *Galaxy Evolution Explorer* (*GALEX*; Martin et al. 2005) space telescope archive. In both records, the UV source is coincident with the optical coordinates of SDSS J2232−0806 within 1.3 arcsec. The UV flux increases by a factor ≈3 between the two epochs and there is also an apparent colour change, with SDSS J2232−0806 appearing bluer in the later observation.

3.3 The spectral energy distribution

3.3.1 Host galaxy contribution to the SED and spectra

Infrared and optical emission from the host galaxy bulge may make a non-negligible contribution to our spectra, particularly in the faint state. It can be seen in our SED (Fig. 5) that the bulge component dominates over the AGN continuum redward of Hβ. However, this is not representative of the host galaxy flux in our spectra, since our narrow 1 arcsec wide slit excludes much of the extended host galaxy emission: a typical bulge diameter of 15 kpc would be ≈3.6 arcsecs across on the sky.

We examined the *HST* images of the source, taken in 2015 September (see Section 3.2.6). The high spatial resolution of the instrument in principle allows us to separate the point-like AGN emission from the more extended host galaxy. We made a visual inspection of the 1D brightness profiles of the source in the two filters. Whereas the source emission in the UVIS filter was PSF-like, the J-band profile had a slightly more extended base than the PSF, suggesting the presence of some light from the host galaxy. Unfortunately, however, the snapshot *HST* exposures are not sufficiently deep to robustly assess the host galaxy emission.

Instead, we can estimate the host galaxy luminosity at 5100 Å in our spectral extraction aperture using the relation of Landt et al. (2011). From a sample of low-redshift ($z \lesssim 0.3$), bright, broad emission line AGN, the authors determined the host galaxy luminosities enclosed in the apertures from stacked *HST* images (see their section 3 and fig. 1). When extracting the WHT spectra, we integrated on average 4.75 arcsec in the spatial direction; the 4.75 arcsec^2 aperture is therefore equivalent to a spatial size of 20 kpc^2 at the source. From the Landt et al. (2011) relation we then estimate $F_{5100\,\text{Å}} \approx 4.2 \times 10^{-17}$ erg s^{-1} cm^{-2} Å^{-1}.

The rms spectrum we constructed in Section 2.2.3 largely removes the non-variable host galaxy contribution, whereas the mean spectrum does not. Therefore, if we assume that the mean AGN emission has the same spectral shape as the variable component, we can estimate the host galaxy contribution by the 'red excess' of the mean spectrum in comparison with the rms. For the host galaxy component we used the 5 Gyr old elliptical galaxy template of Polletta et al. (2007). We add the rms and host galaxy spectra, and rescale the two components until the sum satisfactorily matches the shape of the mean spectrum. From the appropriately scaled galaxy template we determine the mean flux densities in several 150 Å wide windows. The flux densities at 4861, 5007, 5100, and 6563 Å are 4.9, 4.8, 4.6, and 4.8 × 10^{-17} erg s^{-1} cm^{-2} Å^{-1}, respectively; the value at 5100 Å is consistent with the Landt et al. (2011) estimate calculated above, given the uncertainties. The host galaxy contribution to the fluxes at 2800 Å (under Mg II) and at 3000 Å is

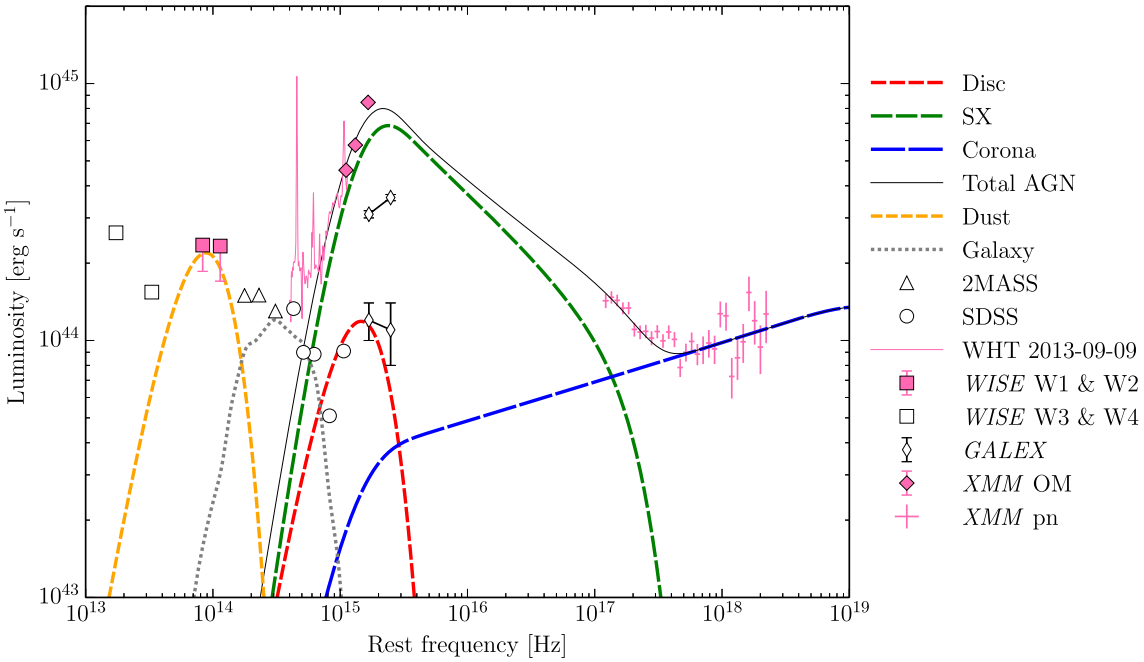

Figure 5. The multiwavelength SED of SDSS J2232−0806. Modelled data are shown in pink: the *XMM–Newton* OM and EPIC-pn data of 2013 December 14; WHT spectrum of 2013 September 9 and *WISE* W1 and W2 IR photometry. Additionally, we show other archival data in white: *WISE* W3 and W4 IR photometry from 2010; 2MASS IR photometry from 1998; SDSS photometry from 2000 and two epochs of *GALEX* UV photometry from 2003 (faint) and 2004 (bright).

negligible. In the rest of this study we correct the AGN continuum fluxes (and hence the emission line EWs) using these values. The emission line EWs recorded in the Tables in the Appendix reflect this correction.

3.3.2 *Accretion flow model*

To model the multiwavelength SED, we use the energy-conserving accretion flow model OPTXAGNF of Done et al. (2012). The model has a standard thin accretion disc from outer radius $R_{\rm out}$ to $R_{\rm cor}$. Interior to $R_{\rm cor}$, the accretion power is divided between soft and hard Comptonization regions. The hard Comptonization region receives the fraction $f_{\rm pl}$ of the available accretion power and produces power-law emission with photon index Γ. The soft Comptonization region upscatters seed photons from the inner edge of the standard thin disc producing soft X-ray emission in excess of the hard coronal power law (this emission is often called the 'soft X-ray excess': SX). The soft Comptonization region is parametrized by its optical depth τ and warm electron temperature $kT_{\rm e}$.

In addition to the direct accretion flow emission, we include a redshifted blackbody (ZBBODY) modelling the hot dust which is sampled by the *WISE* W1 and W2 bands. In Fig. 5 we show the W1 and W2 fluxes corresponding to the earliest *NEOWISE* observation (2014 May 31: the closest in time to the *XMM–Newton* pointing). The downward error bars show the extent of the flux diminution over the observing period. For completeness, the figure also shows the *WISE* W3 and W4 band fluxes, which sample cooler dust. We do not model these data points; the emission may be attributed to AGN- or starlight-heated dust (or some mixture of the two). We show our model SED in Fig. 5, along with the modelled multiwavelength data. Archival data are also shown for illustrative purposes, including two epochs of *GALEX* UV photometry, 2MASS infrared photometry, and the SDSS optical photometry from 2000 during which the AGN was in a deep flux minimum. In Fig. 5 we also show the Polletta et al. (2007) 5 Gyr old elliptical host galaxy template which is normalized to fit the SDSS photometry.

Our SED model has a very prominent soft Comptonization region that emits from the optical/UV into the soft X-ray band. The standard disc component is required only to provide a source of seed photons for the soft Comptonization region in the model calculations and not to fit the shape of the SED itself. We note that Collinson et al. (2018) presented an alternative SED model which contained no soft Comptonization region and in which the optical/UV emission was attributed to a standard accretion disc, with the X-ray spectrum modelled by a single power-law component. This model cannot replicate the curvature in the X-ray spectrum which we detected significantly in Section 3.1.1. Additionally, whilst the single power law of Collinson et al. (2018) has a photon index of $\Gamma = 2.2$, a harder index (such as the $\Gamma = 1.85$ we determine here) would be expected for a system of this Eddington ratio (e.g. Kubota & Done 2018). However, the Eddington ratio determined in both models, $L/L_{\rm Edd} = 0.1$, is the same.

4 THE NATURE OF THE VARIABILITY

We now bring together all of these data sets, and use them to confront two generically distinct scenarios i.e. that the flux changes seen in Fig. 2 are due to reddening by dust, or, that they are a result of an intrinsic variation in the continuum emission from the nuclear region, primarily powered by processes occurring within the accretion disc.

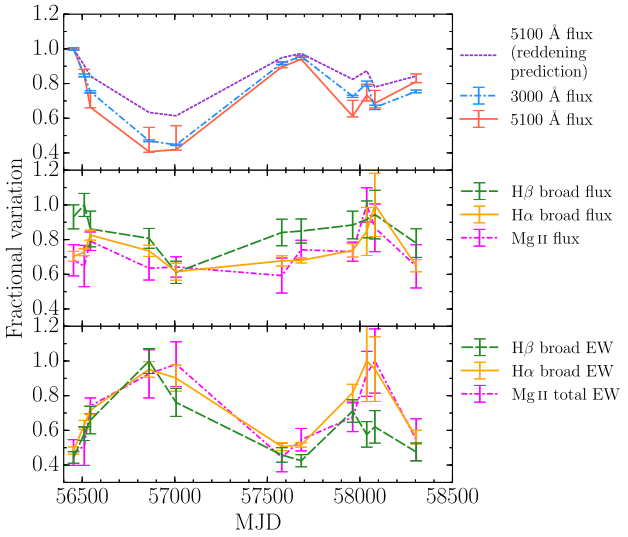

Figure 6. Fractional variations in the 3000 and 5100 Å continuum fluxes and emission line fluxes and EWs over the monitoring period. In the top panel, as well as the observed continuum variations we also show the predicted 5100 Å variations, calculated from the observed 3000 Å variations, on the assumption that these are caused by reddening (see text). The measured 5100 Å fluxes have been corrected for host galaxy contamination using our estimate determined in Section 3.3.1 in the text; the upper error bars indicate the fractional variations calculated with no host galaxy subtraction. For the Balmer lines, values are calculated from the sum of very broad and broad components; the Mg II values are calculated from the whole line profile.

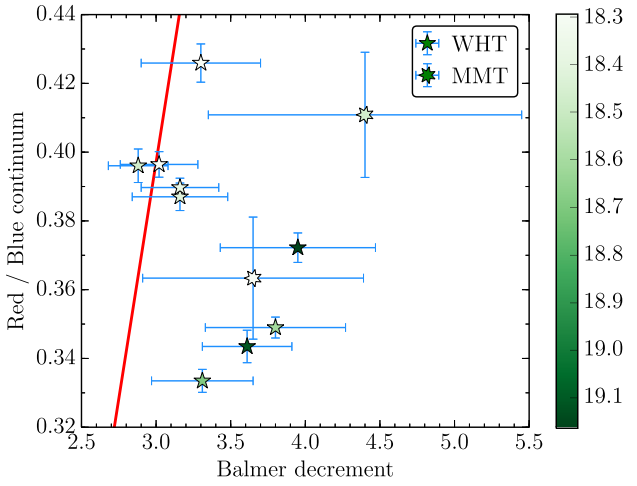

Figure 7. The Balmer decrement (the ratio of broad Hα to broad Hβ fluxes) versus continuum colour (the ratio of 5100 Å to 3000 Å monochromatic fluxes) as measured in each of the 11 optical spectra taken at the WHT and MMT. The colour of the points indicates the equivalent *g*-band magnitude of the spectra calculated in Section 2.2.2: fainter spectra are a darker green. The red line shows the predicted relation for a Cardelli et al. (1989) Galactic reddening curve (assuming the intrinsic Balmer decrement in the case of zero reddening is 2.72).

4.1 Obscuration interpretation

In Fig. 6 we show the relative variations of the continuum fluxes and those of the Mg II and broad Balmer emission lines. The estimated host galaxy flux at 5100 Å has been subtracted from the red continuum flux (see Section 3.3.1). Shorter wavelengths are more sensitive to reddening than longer ones so, under the assumption that the observed changes are due to reddening, we would expect the 5100 Å flux to have a shallower fractional variability curve than at 3000 Å. Based on the Cardelli et al. (1989) Milky Way[10] reddening curve, we have calculated the extinction (A_V) required to cause the observed fractional changes in the blue continuum and then predict the fractional change in the red continuum for the same A_V. We see that the observed AGN flux at 5100 Å shows a significantly greater fractional variability than this prediction, and is broadly consistent with the fractional variations at 3000 Å. There is considerable uncertainty in the AGN continuum 5100 Å fractional flux variations due to the uncertainty in the host galaxy flux subtraction. However, even in the very conservative case when we perform no host galaxy flux subtraction, the 5100 Å fractional flux variability is still inconsistent with that predicted from a reddening law (as indicated by the upper error bars in Fig. 6).

Additionally, we find that the amplitude of line flux changes are somewhat lower than those in the continuum. The 3000 Å flux exhibits variability of more than a factor of 2 whereas the lines show only ≈40 per cent decrease. (Note that our spectroscopic observations did not cover the deep flux minimum seen in the photometric light curve). There is a trend for the emission line EWs to be anticorrelated with the continuum fluxes: increasing when the continuum dims and vice versa. We find that the minimum (maximum) emission line EWs determined over the spectroscopic monitoring period are 570 (1200), 110 (250), and 50 (110) Å for Hα, Hβ, and Mg II, respectively. In the case of a simple screen obscuring both the accretion disc (from which the continuum originates) and BLR (from which the broad lines originate), the EWs of the lines ought not to change since both continuum and line flux at any given wavelength will be suppressed equally. However, if the absorber covers more of the very compact accretion disc than the larger BLR then the EW of the broad lines would be seen to increase.

In Fig. 7 we show how the continuum colour (the ratio of red to blue fluxes) and Balmer decrement have varied together. In the simple scenario of a reddening screen of variable column density obscuring both the BLR and accretion disc, there would be a linear relationship between the Balmer decrement and red/blue continuum flux. We show a reddening vector describing the predicted relationship, again based on the Galactic reddening curve of Cardelli et al. (1989) and positioned so that the Balmer decrement in the case of zero reddening is 2.72 (Gaskell 2017). It can be seen that our data do not follow the trend of this reddening vector so reddening alone cannot explain the observed spectral changes.

4.1.1 *Cloud crossing time-scale*

If the dimming of the AGN continuum and broad emission line fluxes is due to an obscurer moving across our line of sight, then we can predict the time-scale on which such an occultation event would occur. We estimate the BLR size from Bentz et al. (2013)

[10]We note the reddening curves for the Small and Large Magellanic Clouds are very similar to the Milky Way curve for wavelengths >3000 Å which we consider here.

Table 4. Multiwavelength SED model parameters.

Model	Parameter	Units	Description	Value
ZBBODY	$kT_{\rm dust}$	keV (K)	Hot dust temperature	9.30×10^{-5} (1140)
	B.body norm.		Hot dust blackbody normalization	2.43×10^{-5}
HOSTPOL	Gal. norm.		Host galaxy template normalization	2.71×10^{-7}
OPTXAGNF	$\log(L/L_{\rm Edd})$		Eddington ratio	−1.00
	$kT_{\rm e}$	keV	Electron temperature of soft Comptonization region	0.20
	τ		Optical depth of soft Comptonization region	17.3
	Γ		Photon index of power-law coronal emission	1.85
	$f_{\rm pl}$		Fraction of power below $R_{\rm cor}$ emitted in power law	0.32
	$R_{\rm cor}$	$R_{\rm g}$	Inner (standard) accretion disc radius	80.0
	$\log(R_{\rm out})$	$R_{\rm g}$	Outer accretion disc radius	2.01
	$F_{\rm dust}$	erg s^{-1} cm^{-2}	Flux of hot dust blackbody	1.25×10^{-12}
	$F_{\rm disc}$	erg s^{-1} cm^{-2}	Flux of (standard) accretion disc	6.81×10^{-13}
	$F_{\rm SX}$	erg s^{-1} cm^{-2}	Flux of soft Compton emission	8.03×10^{-12}
	$F_{\rm pl}$	erg s^{-1} cm^{-2}	Flux of coronal power-law emission	3.78×10^{-12}
	$F_{\rm UV}$	erg s^{-1} cm^{-2}	AGN flux between 100–4000 Å (rest frame)	7.92×10^{-12}
	$F_{\rm AGN}$	erg s^{-1} cm^{-2}	Total AGN flux	1.25×10^{-11}

Distances are measured in gravitational radii $R_{\rm g} = GM_{\rm BH}/c^2$.

using the equation

$$\log\left(\frac{R_{\rm BLR}}{1\ \text{light day}}\right) = K + \alpha \log\left(\frac{\lambda L_{5100\,\text{Å}}}{10^{44}\ \text{erg s}^{-1}}\right), \quad (4)$$

with values $K = 1.559$ and $\alpha = 0.549$ taken from their 'Clean2+ExtCor' calibration. For the range of $\lambda L_{5100\,\text{Å}}$ observed in our monitoring campaign, the BLR size is ≈40–60 light days.

Following LaMassa et al. (2015) we calculate the crossing time $t_{\rm cross}$ of a cloud occulting the central regions as

$$t_{\rm cross} = 0.07 \left(\frac{R_{\rm orb}}{1\ \text{light day}}\right)^{3/2} \left(\frac{10^8\ \text{M}_\odot}{M_{\rm BH}}\right)^{1/2} \arcsin\left(\frac{R_{\rm src}}{R_{\rm orb}}\right) \text{years}, \quad (5)$$

where $R_{\rm orb}$ is the orbital radius of the cloud and $R_{\rm src}$ is the radius of the emission source being obscured (here the BLR). As a conservative estimate (minimizing the crossing time), we calculate the crossing time for a cloud at the inner edge of the BLR, i.e. $R_{\rm src} = R_{\rm orb} = R_{\rm BLR} \approx 50$ light days. The cloud crossing time at this radius is ≈27 yr, much longer than the dip-and-rise event we observe in the light curve which takes ≈3 yr in the rest frame.

4.2 Intrinsic change interpretation

4.2.1 Dust reverberation

As noted in Section 3.2.1, there is a dip in the infrared light curves, delayed with respect to the optical dip by around 400 d. It can be seen in Fig. 5 that there is negligible host galaxy emission at the wavelengths of the *WISE* W1 and W2 bands (this is true even in the case of a starburst host galaxy, as the IR emission of starlight-heated dust peaks at longer wavelengths). The infrared light curves may therefore be evidence of AGN-heated dust reverberating with the variable intrinsic AGN continuum. However, whilst there is a large (factor ≈3) change in the optical flux, the change in the near-infrared is much more modest (≈30 per cent). The dust emission ought to be a good bolometer of the intrinsic AGN luminosity, so we might expect it to show variability of the same amplitude as seen in the optical. If we attribute the infrared variability to an echo response to variations in the central source, we must account for this discrepancy. Here, we assess whether the observed infrared lag and magnitude changes can be plausibly attributed to dust reverberation.

We can calculate the expected dust reverberation radius from our model SED parameters via

$$R_{\rm dust,rev} = \sqrt{\frac{L_{\rm UV}}{16\pi\sigma T^4}}, \quad (6)$$

where σ is the Stefan–Boltzmann constant and the T is the dust temperature $T = 1140$ K (from Table 4). Since the dust reverberates with the dip in the optical/UV continuum, we take the UV luminosity in the dip to be a factor of 2.5 less than we determined at the time of the *XMM–Newton* observation: $L_{\rm UV,dip} \approx 7.5 \times 10^{44}$ erg s^{-1}. We therefore calculate $R_{\rm dust,rev} \approx 150$ light days. The observed delay between the minimum of the infrared light curve with respect to the optical is ≈428 d, equivalent to ≈335 d in the rest frame, around a factor of 2 greater than $R_{\rm dust,rev}$.

We employ the model tori of Almeyda et al. (2017) to simulate how the dust may respond to a variable, driving optical source. The authors consider the cases of a compact and extended torus, in which the ratio of outer to inner dust cloud radii are 2 and 10, respectively and the inner dust radius in their model is set by dust sublimation. They consider the effects of differing illumination of the torus dust clouds. In the case of isotropic illumination, dust sublimation surface is spherical. In the anisotropically illuminated case, more ionizing flux is emitted in polar directions than in the equatorial plane; the resultant dust sublimation surface is 'bowl-shaped' (see e.g. Kawaguchi & Mori 2010) and the dust near the equatorial plane can survive much closer to the central source than in the isotropic case. The inner dust radius is dependent on the AGN luminosity and the dust sublimation temperature, for which we adopt a value of 1500 K, close to the mean hot dust temperature found by Landt et al. (2011). For SDSS J2232−0806, we calculate the AGN luminosity $L_{\rm AGN}$ from the bolometric flux of our model SED and assume that was 30 per cent greater in the bright state than observed at the time of the *XMM–Newton* observation. We therefore determine that $L_{\rm AGN} \approx 4 \times 10^{45}$ erg s^{-1}. For the isotropic case, $R_{\rm in} = R_{\rm sub} \approx 0.7$ pc (≈800 light days) whereas for the anisotropic case $R_{\rm in} = R_{\rm sub}(\theta = 90^\circ) \approx 0.25$ pc (≈300 light days).

To construct our driving light curve, we interpolate between the LT optical photometry points to create a continuous light curve, which we then smooth to remove the short-term, stochastic

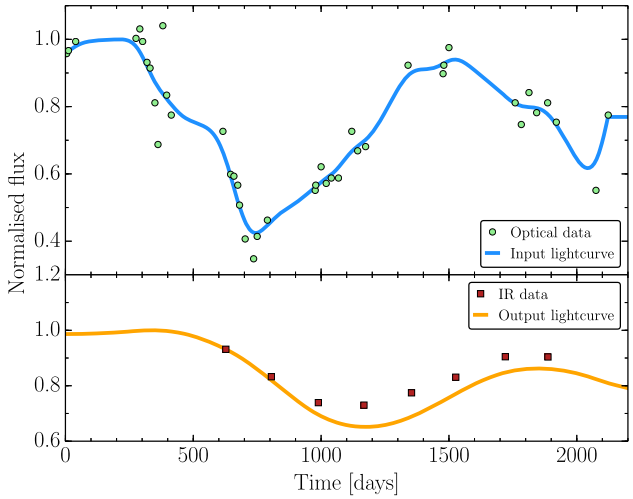

Figure 8. The simulated dust response to the variable optical source. *Top:* Our optical data (LT g-band photometry) are shown as green circles. We linearly interpolate between these and smooth the result to create an input optical light curve (the blue line). *Bottom:* We convolve the input light curve with an impulse response function to predict the infrared light curve (the orange line). The impulse response function was calculated by Almeyda et al. (2017) for an anisotropically illuminated, radially extended ($R_{\rm out}/R_{\rm in} = 10$) distribution of dust clouds in a torus of angular width $\sigma = 45^\circ$ with $R_{\rm dust} =$ 250 light days and viewed at a polar angle of $\theta_{\rm obs} = 45^\circ$. The *WISE* W1 (3.4 μm) photometry is shown as red squares and the data are normalized such that the first point falls on the predicted light curve.

variability and retain only the shape of the longer term, systematic, large-amplitude changes. Almeyda et al. (2017) provide their impulse response functions at 3.6 μm for a torus viewed at a polar angle of $\theta_{\rm obs} = 45^\circ$ (see their fig. 8). We convolve our optical light curve with four response functions (for compact/extended, isotropically/anisotropically illuminated tori) and compare the simulated dust responses with our *WISE* W1 data. We find that the response functions for the isotropically illuminated tori produce much longer lags than is observed. The lags for the anisotropically illuminated tori are shorter because the of the closer proximity of the dust to the optical/UV source, and are in much better agreement with our data. The simulated responses for the compact tori are too deep, an extended distribution is required to smear out the response and reduce its amplitude. In Fig. 8 we show the simulated dust response in the case of an extended, anisotropically illuminated torus. In this figure we have slightly decreased $R_{\rm in}$ to 250 light days from the 300 light days calculated from $L_{\rm AGN}$, to better match the observed light curve.

4.2.2 *Accretion disc variability time-scales*

We now assess the predicted time-scales for the transmission of changes through a standard thin accretion disc. In Section 3.3.2 we determined the outer radius of the accretion disc to be $R \sim 100\,R_{\rm g}$. For a disc of this size, the dynamical time-scale is

$$t_{\rm dyn} \approx \left(\frac{R^3}{GM_{\rm BH}}\right)^{1/2} \approx 10\ {\rm d}; \quad (7)$$

the thermal time-scale is

$$t_{\rm therm} \approx \frac{t_{\rm dyn}}{\alpha} \approx 3\ {\rm months}, \quad (8)$$

where $\alpha \approx 0.1$ is the disc viscosity parameter; the viscous time-scale is

$$t_{\rm visc} \approx \frac{t_{\rm dyn}}{\alpha}\left(\frac{H}{R}\right)^{-2} \approx 1\ {\rm Myr} \quad (9)$$

where H/R is the ratio of the disc's thickness to its radius. As Noda & Done (2018) found for Mrk 1018, we find that for SDSS J2232−0806 the dynamical and thermal time-scales are too short compared with the observed variability time-scale and the viscous time-scale is far too long.

5 DISCUSSION

5.1 An extrinsic cause of variability

The hypothesis of an extrinsic cause of the variability (i.e. variable obscuration) is inconsistent with the observations in several important respects:

(i) The continuum colour change is inconsistent with reddening since we see approximately equal fractional flux change in the red as in the blue (Fig. 6). Even if we perform no subtraction of host galaxy flux at 5100 Å the source still exhibits significantly more variability in the red than would be inferred from the blue, assuming that reddening causes the variability. We note that the choice of reddening curve makes very little difference at the wavelengths we studied.

(ii) The Balmer decrements do not change consistently (Fig. 7), although this test is less compelling given the substantial uncertainties in the measurements. However, since the emission line EWs change, the obscurer cannot be covering both the accretion disc and all of the BLR.

(iii) We are able to place an upper limit of 7×10^{19} cm^{-2} on the intrinsic column density from the *XMM–Newton* X-ray observation, although a column of $\approx 4 \times 10^{20}$ cm^{-2} would be required to produce the observed 30 per cent drop in the g-band flux. Furthermore, Maiolino et al. (2001) reported that the dust reddening of AGNs is generally much lower than one would calculate from the gas column density probed by X-rays, assuming a Galactic dust-to-gas ratio and extinction curve, as we do here. If this were the case for SDSS J2232−0806, an even greater $N_{\rm H}^{\rm int}$ would be predicted, increasing the discrepancy with the X-ray observations.

(iv) The time-scale for obscuration is far too long. We calculate that the crossing time of an obscuring cloud at the inner BLR radius is ≈27 yr, much longer than the 3 yr we observe. Furthermore, this scenario does not explain how a dust cloud could survive relatively near to the central ionizing source.

(v) Variable obscuration fails to explain the observed variations in the infrared. Since mid-infrared wavelengths are less sensitive to reddening than the optical, a 0.26 mag change at 3.4 μm would imply a simultaneous 5.5 mag change in the g band which is clearly inconsistent with our data. If the obscurer were exterior to the torus, it would be at an extremely large orbital radius and the crossing time would be even longer than calculated above. If the obscurer were interior to the torus it would need to be implausibly close to the accretion disc (to explain the lag), and implausibly large (to obscure a sufficient fraction of the AGN flux as seen by the dust).

5.2 An intrinsic cause of variability

Having ruled out the possibility of an extrinsic change, we consider that the variability is due to an intrinsic change in the luminosity of the accreting matter. In Section 4.2.1 we simulated dust responses

to a driving optical continuum. Our intention with this test was not to infer the properties of the torus but to examine the plausibility that the infrared emission reverberates with the optical. Although we have tested only a few points in the dust response parameter space presented by Almeyda et al. (2017), the simulated IR light curve shown in Fig. 8 captures both the lag and shape of the observed IR variability very well. It is therefore very plausible that the IR emission exhibits a genuine light echo of the optical variability.

Sheng et al. (2017) studied a sample of changing-look quasars that exhibited significant, large-amplitude ($|\Delta W1|$ or $|\Delta W2| > 0.4$ mag) mid-infrared variability. Since mid-infrared wavelengths are not strongly affected by dust extinction, the mid-infrared variability would imply much greater changes in the optical than observed if both were due to variable obscuration. They also found that the time-scales for dust cloud obscuration of the torus were far too long whereas the observed lags between infrared and optical were consistent with those expected for hot dust reverberation. They concluded that in all of the 10 objects they investigated that the variability was intrinsic in nature. We argue that SDSS J2232−0806 shows the same behaviour.

The rms spectrum (Fig. 3) indicates different variability behaviours of the observed emission lines. The broad Balmer emission lines appear as strong features in the rms spectrum, highlighting their significant variability. The He II λ4686 and He I λ5876 emission lines are known to respond strongly and rapidly to changes in the continuum, and are also prominent. However, Mg II almost completely disappears in the rms spectrum, indicating that it has varied very little over our monitoring campaign. Both Zhu, Sun & Wang (2017) and Sun et al. (2015) have studied the reverberation of Mg II in quasars observed multiple times as part of the SDSS. Zhu et al. (2017) noted that Mg II responds relatively weakly to changes in the 3000 Å continuum. Sun et al. (2015) compared the Mg II and Hβ emission line variability and found that Mg II is ≈1.5 times less responsive to changes in the continuum than Hβ. It is not currently known why this is the case. It may be that Mg II is emitted over a much larger range of radii than Hβ and so its response is more strongly diluted. Alternatively, differences in the excitation/de-excitation mechanisms or in the optical depths of the two lines are also possible explanations.

Whilst we favour an intrinsic cause of the variability over an extrinsic cause, our calculations in Section 4.2.2 show that the predicted time-scales for such changes do not match the observations. It has been known for some time that large-amplitude variability of AGNs occurs on time-scales much shorter than predicted for thin, viscous accretion discs. Dexter & Begelman (2019) address this so-called 'quasar viscosity crisis' (Lawrence 2018) and propose that all AGN accretion discs may be 'magnetically elevated' and have a much greater scale height than is typically assumed, dramatically reducing the predicted variability time-scales. Alternative models have recently been developed to explain the extreme variability seen in individual sources. Ross et al. (2018) presented a scenario for the CLQ SDSS J110057.70−005304.5 in which a dramatic change in magnetic torque at the innermost disc radii resulted in a collapse of the UV continuum and triggered a cooling/heating front propagating through the disc, out to ∼200 R_g. Taking a different approach, Noda & Done (2018) determined that Mrk 1018 underwent a spectral state transition , similar to those seen in stellar-mass black hole binaries (BHBs). Whilst scaling up to AGN size scales by BH mass predicts too long variability time-scales in AGN, the authors discuss ways in which scalings between BHBs and AGN may break down.

5.3 SDSS J2232−0806 in the context of other hypervariabale AGN

Both MacLeod et al. (2018) and Rumbaugh et al. (2018) have recently presented the results of systematic searches of long-term extremely variable quasars (EVQs: sources with $|\Delta g| > 1$ mag) from archival optical data. Rumbaugh et al. (2018) found that EVQs account for ≈30–50 per cent of all quasars and that the EVQs had systematically lower $L/L_{\rm Edd}$ than the parent sample of 'normal' quasars. MacLeod et al. (2018) presented follow-up spectroscopic observations of a sample of EVQs and were able to confirm that ≈20 per cent of these were CLQs. The authors compared the CLQs with a luminosity- and redshift-matched, lesser variable control sample and again found that CLQs on average have lower $L/L_{\rm Edd}$ than their less-variable counterparts. Both studies suggested that EVQs and CLQs represent the extremes of a tail of 'normal' quasar variability. At the far range of this tail, some sources exhibit nearly an order of magnitude change in optical flux over a baseline of ∼10 yr. Compared to many of these changing-look AGN, the continuum flux change we observed during our monitoring of SDSS J2232−0806 is modest. Its $\log(L/L_{\rm Edd}) = -1$ is slightly higher than the peaks of the distributions of CLQs and EVQs (which occur at $\log(L/L_{\rm Edd}) \approx -1.5$, see fig. 6 of MacLeod et al. 2018) although it is consistent with the range of values for all of the populations shown (CLQs, EVQs, the less-variable control sample and all 105783 of the SDSS DR7 quasars). Assuming the bolometric flux of the source decreases proportionally to the observed optical, we can estimate that the accretion rate of SDSS J2232−0806 drops to ∼a few per cent of Eddington in the faint state.

Elitzur & Ho (2009) proposed a disc wind model of the BLR in which AGN with a very low $L/L_{\rm Edd}$ are unable to support a BLR. After studying a sample of low-luminosity AGN, they determined that the BLR disappears when the AGN luminosity drops below a critical value, $L_{\rm AGN} \lesssim 5 \times 10^{39} (M_{\rm BH}/10^7 {\rm M}_\odot)^{2/3}$ erg s^{-1}. MacLeod et al. (2018) found that their CLQs were distributed close to this critical value and likely dropped below it in their faint state, naturally explaining the disappearance of the broad emission lines. Whilst the broad Balmer emission lines in SDSS J2232−0806 do weaken in response to a dimming continuum, the source does not satisfy the criterion of a changing-look AGN because these lines have not been observed to disappear. The source was in a deep minimum in 2000, and it is likely that the host galaxy emission dominates all of the SDSS bands except *u*. Its UV flux in this epoch was ≈4 times fainter than when it was observed by *XMM–Newton*. Assuming the bolometric flux was also 4 times fainter, its luminosity in 2000 was $\approx 8 \times 10^{44}$ erg s^{-1}. For the BH mass of SDSS J2232−0806, the critical luminosity for a BLR in the disc-wind model is $\approx 4 \times 10^{40}$ erg s^{-1}, so the broad lines ought to have been visible even in this deep minimum. Therefore, we suggest that SDSS J2232−0806 lies on the sequence of quasar variability, being highly variable whilst its mass accretion rate is too high for it to undergo a changing-look transition.

Whereas optically variable AGN are typically 'bluer-when-brighter' (e.g. Wilhite et al. 2005; Rumbaugh et al. 2018) we do not see strong evidence of that behaviour in our optical monitoring of SDSS J2232−0806. Having corrected the longer wavelength fluxes for host galaxy contamination, we show in Fig. 6 that the fractional variabilities in the blue and red are similar (i.e. there is no significant colour change). In Fig. 3 we show that the shape of the rms spectrum is very similar to that of the mean spectrum at the shorter wavelengths less affected by host galaxy contamination. We note that Wilhite et al. (2005) used a sample of higher redshift

quasars than SDSS J2232−0806 ($z > 0.5$) so they probed further into the rest frame UV than we do. The authors show that there is a spectral break in the variability of their sample around 2500 Å in the rest frame, with wavelengths shorter than this being more strongly variable. We may not see evidence of a spectral shape change in SDSS J2232−0806 because our spectra do not sample below 2500 Å. Furthermore, we see in SDSS J2232−0806 that changes in the red and blue optical continuum (predominantly emitted from larger/smaller radii, respectively) appear to occur in tandem. We do not see a delay in the variations between the red and blue optical emission, indicative of a heating/cooling front propagating through the disc, such as in the model described by Ross et al. (2018).

5.4 Prospects for future work

Our observing campaign was fortunate to have recorded a dramatic dimming and brightening event of SDSS J2232−0806. There is some evidence that similar events have occurred in its past. The source appears to have been in a relatively bright state when observed photographically in 1988 but was in a deep minimum in the SDSS observation of 2000. The Catalina light curve suggests another dip occurred between 2005–2007 (see Fig. 1). As noted by MacLeod et al. (2018), past hypervariable behaviour is an indicator of future events. Future monitoring of this source is desirable as we may capture other interesting episodes of variability.

New X-ray and UV observations would be highly beneficial in further investigating the nature of the variability. Sampling both sides of the peak of the accretion disc emission peak would enable us to parametrize the changing energetics during a variability episode and determine whether SDSS J2232−0806 undergoes spectral state changes as seen in e.g. Mrk 1018 (Noda & Done 2018). The ability of UV and X-rays to probe the innermost regions would enable us to determine whether some 'collapse' of the UV emission occurs as seen in e.g. SDSS J110057.70−005304.5 (Ross et al. 2018).

6 CONCLUSIONS

Our recent optical photometric and spectroscopic monitoring campaign on the hypervariable AGN SDSS J2232−0806 has recorded one dimming and brightening episode with a factor ≈3 flux change over 4 yr. Whilst the observed variability of the source is modest compared to that seen in changing-look AGN, it is extreme compared to the broader AGN population. We have been able to demonstrate that variable obscuration does not explain the observed spectral changes, nor does it fit the observed time-scales for variability in the optical or near-infrared. An intrinsic change in the AGN luminosity is therefore a likelier explanation, although the observed changes are much more rapid than the theoretical accretion disc viscous time-scale. SDSS J2232−0806 is one of a growing number of objects which challenge our models of viscous accretion discs. Whilst we are unable to determine the cause of the intrinsic luminosity change, X-ray and UV monitoring of future episodes should greatly improve our understanding of the processes at work.

ACKNOWLEDGEMENTS

DK acknowledges the receipt of a UK Science and Technology Facilities Council (STFC) studentship (ST/N50404X/1). DK and MJW acknowledge support from the STFC grant ST/P000541/1. Thanks to Michael Fausnaugh for his assistance in the use of MAPSPEC. Thanks also to Ra'ad Mahmoud, Raj Sathyaprakash, Chris Done, David Rosario, and Brad Peterson for useful discussions. In this research we have made use of the following:

(i) data from the William Herschel Telescope, operated on the island of La Palma by the Isaac Newton Group of Telescopes in the Spanish Observatorio del Roque de los Muchachos of the Instituto de Astrofísica de Canarias;

(ii) data from the Liverpool Telescope, operated on the island of La Palma by Liverpool John Moores University in the Spanish Observatorio del Roque de los Muchachos of the Instituto de Astrofísica de Canarias with financial support from the STFC;

(iii) observations obtained at the MMT Observatory, a joint facility of the Smithsonian Institution and the University of Arizona;

(iv) data products from the *WISE* mission, which is a joint project of the University of California, Los Angeles, and the Jet Propulsion Laboratory/California Institute of Technology, and *NEOWISE*, which is a project of the Jet Propulsion Laboratory/California Institute of Technology. *WISE* and *NEOWISE* are both funded by the National Aeronautics and Space Administration (NASA);

(v) data from and software developed for *XMM–Newton*, an ESA science mission with instruments and contributions directly funded by ESA Member States and NASA;

(vi) observations made with the NASA *Galaxy Evolution Explorer*. *GALEX* is operated for NASA by the California Institute of Technology under NASA contract NAS5-98034;

(vii) data products from the Two Micron All Sky Survey (2MASS), which is a joint project of the University of Massachusetts and the Infrared Processing and Analysis Center/California Institute of Technology, funded by NASA and the National Science Foundation;

(viii) data from SDSS: funding for the SDSS and SDSS-II has been provided by the Alfred P. Sloan Foundation, the Participating Institutions, the National Science Foundation, the U.S. Department of Energy, the National Aeronautics and Space Administration, the Japanese Monbukagakusho, the Max Planck Society, and the Higher Education Funding Council for England. The SDSS Web Site is http://www.sdss.org/;

(ix) data from Pan-STARRS-1: the Pan-STARRS-1 Surveys (PS1) have been made possible through contributions of the Institute for Astronomy, the University of Hawaii, the Pan-STARRS Project Office, the Max-Planck Society and its participating institutes, the Max Planck Institute for Astronomy, Heidelberg and the Max Planck Institute for Extraterrestrial Physics, Garching, The Johns Hopkins University, Durham University, the University of Edinburgh, Queen's University Belfast, the Harvard-Smithsonian Center for Astrophysics, the Las Cumbres Observatory Global Telescope Network Incorporated, the National Central University of Taiwan, the Space Telescope Science Institute, the National Aeronautics and Space Administration under Grant No. NNX08AR22G issued through the Planetary Science Division of the NASA Science Mission Directorate, the National Science Foundation under Grant No. AST-1238877, the University of Maryland, and Eotvos Lorand University (ELTE);

(x) data obtained from the SuperCOSMOS Science Archive, prepared and hosted by the Wide Field Astronomy Unit, Institute for Astronomy, University of Edinburgh, which is funded by the UK STFC;

(xi) the SPECTRES spectral resampling tool (Carnall 2017);

(xii) Doug Welch's Excellent Absorption Law Calculator (http://www.dougwelch.org/Acurve.html);

(xiii) Ned Wright's Cosmology Calculator (Wright 2006).

REFERENCES

Almeyda T., Robinson A., Richmond M., Vazquez B., Nikutta R., 2017, ApJ, 843, 3
Arnaud K. A., 1996, in Jacoby G. H., Barnes J., eds, ASP Conf. Ser. Vol. 101, Astronomical Data Analysis Software and Systems V. Astron. Soc. Pac., San Francisco, p. 17
Bentz M. C. et al., 2013, ApJ, 767, 149
Bohlin R. C., Savage B. D., Drake J. F., 1978, ApJ, 224, 132
Bruce A. et al., 2017, MNRAS, 467, 1259
Bruhweiler F., Verner E., 2008, ApJ, 675, 83
Cannon R. D., 1975, Proc. Astron. Soc. Aust., 2, 323
Cardelli J. A., Clayton G. C., Mathis J. S., 1989, ApJ, 345, 245
Carnall A. C., 2017, preprint (arXiv:1705.05165)
Chambers K. C. et al., 2016, preprint (arXiv:1612.05560)
Collinson J. S. et al., 2018, MNRAS, 474, 3565
Dexter J., Begelman M. C., 2019, MNRAS, 483, L17
Dickey J. M., Lockman F. J., 1990, ARA&A, 28, 215
Done C., Davis S. W., Jin C., Blaes O., Ward M., 2012, MNRAS, 420, 1848
Elitzur M., Ho L. C., 2009, ApJ, 701, L91
Elvis M. et al., 2012, ApJ, 759, 6
Fausnaugh M. M., 2017, PASP, 129, 024007
Gaskell C. M., 2017, MNRAS, 467, 226
Gezari S. et al., 2017, ApJ, 835, 144
Goodrich R. W., 1995, ApJ, 440, 141
Hambly N. C. et al., 2001, MNRAS, 326, 1279
Jin C., Ward M., Done C., 2012, MNRAS, 422, 3268
Katebi R. et al., 2018, preprint (arXiv:1811.03694)
Kawaguchi T., Mori M., 2010, ApJ, 724, L183
Kubota A., Done C., 2018, MNRAS, 480, 1247
LaMassa S. M. et al., 2015, ApJ, 800, 144
Landt H., Elvis M., Ward M. J., Bentz M. C., Korista K. T., Karovska M., 2011, MNRAS, 414, 218
Lawrence A. et al., 2016, MNRAS, 463, 296
Lawrence A., 2018, Nat. Astron., 2, 102
Lu K.-X., Zhao Y., Bai J.-M., Fan X.-L., 2019, MNRAS, 483, 1722
MacLeod C. L. et al., 2012, ApJ, 753, 106
MacLeod C. L. et al., 2016, MNRAS, 457, 389
MacLeod C. L. et al., 2018, preprint (arXiv:1810.00087)
Magnier E. A. et al., 2013, ApJS, 205, 20
Maiolino R., Marconi A., Salvati M., Risaliti G., Severgnini P., Oliva E., La Franca F., Vanzi L., 2001, A&A, 365, 28
Martin D. C. et al., 2005, ApJ, 619, L1
McHardy I. M. et al., 2018, MNRAS, 480, 2881
Mejía-Restrepo J. E., Trakhtenbrot B., Lira P., Netzer H., Capellupo D. M., 2016, MNRAS, 460, 187
Noda H., Done C., 2018, MNRAS, 480, 3898
Osterbrock D. E., Ferland G. J., 2006, Astrophysics of Gaseous Nebulae and Active Galactic nuclei, 2ndedn. University Science Books, Mill Valley, CA
Parker M. L. et al., 2016, MNRAS, 461, 1927
Pei L. et al., 2017, ApJ, 837, 131
Peterson B. M. et al., 2004, ApJ, 613, 682
Polletta M. et al., 2007, ApJ, 663, 81
Ross N. P. et al., 2018, MNRAS, 480, 4468
Ruan J. J. et al., 2016, ApJ, 826, 188
Rumbaugh N. et al., 2018, ApJ, 854, 160
Runnoe J. C. et al., 2016, MNRAS, 455, 1691
Schmidt K. B., Rix H.-W., Shields J. C., Knecht M., Hogg D. W., Maoz D., Bovy J., 2012, ApJ, 744, 147
Sheng Z., Wang T., Jiang N., Yang C., Yan L., Dou L., Peng B., 2017, ApJ, 846, L7
Skrutskie M. F. et al., 2006, AJ, 131, 1163
Stern D. et al., 2018, ApJ, 864, 27
Sun M. et al., 2015, ApJ, 811, 42
van Groningen E., Wanders I., 1992, PASP, 104, 700
Vanden Berk D. E. et al., 2001, AJ, 122, 549
Wang J., Xu D. W., Wei J. Y., 2018, ApJ, 858, 49
Wilhite B. C., Vanden Berk D. E., Kron R. G., Schneider D. P., Pereyra N., Brunner R. J., Richards G. T., Brinkmann J. V., 2005, ApJ, 633, 638
Wright E. L., 2006, PASP, 118, 1711
Wright E. L. et al., 2010, AJ, 140, 1868
Yang Q. et al., 2018, ApJ, 862, 109
Zhu D., Sun M., Wang T., 2017, ApJ, 843, 30
Zuo W., Wu X.-B., Liu Y.-Q., Jiao C.-L., 2012, ApJ, 758, 104

APPENDIX A: OPTICAL SPECTRAL FITTING RESULTS

Table A1. Balmer, [O III], and [N II] emission line measurements.

					Hα				
Date	Scale	Δv_{vb}	W_b	W_n	f_{vb} × 10^{-15}	f_b × 10^{-14}	f_n × 10^{-15}	f_{tot} × 10^{-14}	EW_{vb+b}
2013-06-10	1.446	+800 ± 700	4460 ± 50	480 ± 10	3 ± 2	5.05 ± 0.08	1.5 ± 0.1	5.5 ± 0.2	570 ± 20
2013-08-07	1.584	+1900 ± 700	4530 ± 60	550 ± 10	3 ± 1	5.20 ± 0.08	1.8 ± 0.1	5.7 ± 0.2	750 ± 30
2013-09-09	1.046	+1300 ± 800	4280 ± 50	510 ± 10	9 ± 2	5.4 ± 0.1	1.81 ± 0.08	6.5 ± 0.2	850 ± 30
2014-07-23	1.173	+800 ± 700	4200 ± 60	480 ± 10	6 ± 2	4.97 ± 0.09	1.59 ± 0.09	5.7 ± 0.2	1130 ± 50
2014-12-16	1.076	+2000 ± 500	4300 ± 50	570 ± 20	5 ± 4	4.2 ± 0.1	1.7 ± 0.1	4.8 ± 0.4	1070 ± 90
2016-07-09	1.344	≤700	4600 ± 100	490 ± 10	3 ± 2	4.8 ± 0.1	1.47 ± 0.06	5.3 ± 0.2	600 ± 30
2016-10-22	0.706	+1800 ± 500	4510 ± 40	540 ± 10	3 ± 1	4.86 ± 0.05	1.48 ± 0.05	5.3 ± 0.1	610 ± 10
2017-07-27	1.022	+1800 ± 8000	4500 ± 100	470 ± 10	4 ± 3	5.2 ± 0.1	1.43 ± 0.07	5.7 ± 0.3	970 ± 60
2017-10-11	1.152	+1900	3670 ± 90	700 ± 200	1.2 ± 0.3	5 ± 1	1.7 ± 0.4	7 ± 1	1200 ± 300
2017-11-24	1.316	+1900	4000 ± 500	500 ± 100	2.1 ± 0.7	6 ± 1	1.1 ± 0.4	8 ± 1	1100 ± 200
2018-07-05	1.093	+1800 ± 800	4560 ± 80	490 ± 30	4 ± 3	4.5 ± 0.1	1.5 ± 0.1	5.1 ± 0.3	660 ± 40

Table A2. Balmer, [O III], and [N II] emission line measurements (continued).

	[NII] λ6583	Hβ						[OIII] λ5007	
Date	f × 10^{-16}	f_{vb} × 10^{-15}	f_b × 10^{-14}	f_n × 10^{-16}	f_{tot} × 10^{-14}	EW_{vb+b}	BD_{vb+b}	f × 10^{-15}	EW
2013-06-10	5.7 ± 0.1	3 ± 1	1.46 ± 0.09	2.3 ± 0.1	1.8 ± 0.1	112 ± 8	3.0 ± 0.3	3.2 ± 0.5	21 ± 3
2013-08-07	6.5 ± 0.2	3 ± 1	1.58 ± 0.04	2.7 ± 0.2	1.9 ± 0.1	150 ± 10	2.9 ± 0.2	3.5 ± 0.1	28 ± 8
2013-09-09	6.0 ± 0.1	3 ± 2	1.32 ± 0.05	2.7 ± 0.1	1.7 ± 0.2	170 ± 20	3.8 ± 0.5	3.7 ± 0.2	40 ± 20
2014-07-23	5.7 ± 0.1	3 ± 1	1.21 ± 0.05	2.4 ± 0.1	1.6 ± 0.1	250 ± 20	3.6 ± 0.3	3.4 ± 0.6	56 ± 9
2014-12-16	6.6 ± 0.2	3 ± 1	0.83 ± 0.03	2.6 ± 0.2	1.2 ± 0.1	190 ± 20	4.0 ± 0.5	3.3 ± 0.8	50 ± 10
2016-07-09	5.7 ± 0.2	3 ± 1	1.32 ± 0.09	2.2 ± 0.1	1.6 ± 0.2	120 ± 10	3.2 ± 0.3	3.1 ± 0.4	24 ± 3
2016-10-22	6.4 ± 0.2	3 ± 1	1.34 ± 0.06	2.20 ± 0.08	1.7 ± 0.1	110 ± 10	3.2 ± 0.3	3.3 ± 0.2	23 ± 2
2017-07-27	5.4 ± 0.1	3 ± 1	1.41 ± 0.08	2.1 ± 0.1	1.7 ± 0.2	180 ± 20	3.3 ± 0.3	3.2 ± 0.5	35 ± 5
2017-10-11	8 ± 2	5 ± 2	1.3 ± 0.1	2.5 ± 0.6	1.8 ± 0.2	150 ± 20	3.7 ± 0.7	2.5 ± 0.6	22 ± 6
2017-11-24	6 ± 2	5 ± 2	1.3 ± 0.2	1.6 ± 0.6	1.7 ± 0.3	160 ± 20	4.4 ± 1.0	1.8 ± 0.5	16 ± 4
2018-07-05	5.7 ± 0.4	3 ± 1	1.19 ± 0.09	2.2 ± 0.2	1.5 ± 0.2	120 ± 10	3.3 ± 0.4	3.4 ± 0.8	29 ± 6

'Scale' is the flux scaling factor applied to each spectrum, including both internal and absolute scalings (see Section 2.2.2 in the text). Subscripts 'vb', 'b', and 'n' refer to the very broad, broad, and narrow emission line components, respectively, and 'tot' is the total. Δv_{vb} is the velocity offset (in km s^{-1}) of the very broad emission line components relative to the narrower components; positive values indicate a redward offset. Fluxes f in erg s^{-1} cm^{-2}; widths 'W' are FWHM in km s^{-1} and equivalent widths 'EW' are in Å. 'BD' is the Balmer decrement Hα/Hβ.

Table A3. Mg II emission line measurements.

Date	W_{vb}	f_{vb} × 10^{-14}	W_b	f_b × 10^{-14}	W_{tot}	f_{tot} × 10^{-14}	EW_{tot}
2013-06-10	9000 ± 800	2.2 ± 0.5	3300 ± 300	1.5 ± 0.2	4200 ± 400	3.7 ± 0.5	51 ± 8
2013-08-07	9000 ± 1000	2.0 ± 0.6	3100 ± 500	1.5 ± 0.3	3900 ± 500	3.5 ± 0.7	60 ± 10
2013-09-09	10000 ± 600	2.4 ± 0.3	3400 ± 100	1.9 ± 0.1	4100 ± 200	4.3 ± 0.3	80 ± 10
2014-07-23	9000 ± 700	1.5 ± 0.3	3600 ± 200	2.0 ± 0.2	4000 ± 200	3.5 ± 0.4	100 ± 10
2014-12-16	8400 ± 600	2.1 ± 0.3	3100 ± 200	1.4 ± 0.1	4000 ± 300	3.5 ± 0.3	110 ± 10
2016-07-09	9000 ± 1000	1.9 ± 0.5	3300 ± 400	1.3 ± 0.2	4200 ± 500	3.2 ± 0.6	50 ± 10
2016-10-22	11000 ± 500	2.4 ± 0.3	3400 ± 200	1.7 ± 0.1	4300 ± 200	4.0 ± 0.3	59 ± 7
2017-07-27	9900 ± 700	2.0 ± 0.3	3600 ± 200	2.0 ± 0.1	4200 ± 200	4.0 ± 0.3	73 ± 9
2017-10-11	14000 ± 1300	3.2 ± 0.5	3500 ± 200	2.3 ± 0.2	4200 ± 300	5.5 ± 0.5	100 ± 10
2017-11-24	11000 ± 1700	2.9 ± 0.7	3300 ± 300	1.8 ± 0.3	4200 ± 500	4.7 ± 0.7	110 ± 20
2018-07-05	9000 ± 1000	2.0 ± 0.6	3300 ± 400	1.5 ± 0.3	4200 ± 500	3.5 ± 0.7	60 ± 10

Subscripts 'vb' and 'b' refer to the very broad and broad emission line components, respectively, and 'tot' is the total. Fluxes f in erg s^{-1} cm^{-2}; widths 'W' are FWHM in km s^{-1} and equivalent widths 'EW' are in Å.

This paper has been typeset from a TEX/LATEX file prepared by the author.